OPEN ACCESS
IOP Publishing
Superconductor Science and Technology
Supercond. Sci. Technol. **33** (2020) 044005 (12pp)
https://doi.org/10.1088/1361-6668/ab7053

MoRe/YBCO Josephson junctions and π-loops

M I Faley[1], P Reith[2], C D Satrya[2], V S Stolyarov[3,4], B Folkers[2], A A Golubov[2,3], H Hilgenkamp[2] and R E Dunin-Borkowski[1,5]

[1] Peter Grünberg Institute 5, Forschungszentrum Jülich GmbH, 52425 Jülich, Germany
[2] Faculty of Science and Technology, MESA+ Institute for Nanotechnology, University of Twente, 7500 AE Enschede, The Netherlands
[3] The Moscow Institute of Physics and Technology, 141700 Dolgoprudny, Moscow Region, Russia
[4] Dukhov Research Institute of Automatics (VNIIA), 127055 Moscow, Russia
[5] Ernst Ruska-Centre for Microscopy and Spectroscopy with Electrons, Forschungszentrum Jülich GmbH, D-52425 Jülich, Germany

E-mail: m.faley@fz-juelich.de

Received 22 October 2019, revised 9 January 2020
Accepted for publication 27 January 2020
Published 17 February 2020

Abstract

We have developed Josephson junctions between the *d*-wave superconductor $YBa_2Cu_3O_{7-x}$ (YBCO) and the *s*-wave $Mo_{0.6}Re_{0.4}$ (MoRe) alloy superconductor (*ds*-JJs). Such *ds* Josephson junctions are of interest for superconducting electronics making use of incorporated π-phase shifts. The *I(V)*-characteristics of the *ds*-JJs demonstrate a twice larger critical current along the [100] axis of the YBCO film compared to similarly-oriented *ds*-JJs made with a Nb top electrode. The characteristic voltage I_cR_n of the YBCO–Au–MoRe *ds*-JJs is 750 μV at 4.2 K. The *ds*-JJs that are oriented along the [100] or [010] axes of the YBCO film exhibit a 200 times higher critical current than similar *ds*-JJs oriented along the [110] axis of the same YBCO film. A critical current density $J_c = 20\,\mathrm{kA\,cm^{-2}}$ at 4.2 K was achieved. Different layouts of π-loops based on the novel *ds*-JJs were arranged in various mutual coupling configurations. Spontaneous persistent currents in the π-loops were investigated using scanning SQUID microscopy. Magnetic states of the π-loops were manipulated by currents in integrated bias lines. Higher flux states up to $\pm 2.5\Phi_0$ were induced and stabilized in the π-loops. Crossover temperatures between thermally activated and quantum tunneling switching processes in the *ds*-JJs were estimated. The demonstrated ability to stabilise and manipulate states of π-loops paves the way towards new computing concepts such as quantum annealing computing.

Keywords: *d*-wave superconductor, Josephson junction, scanning SQUID microscopy, π-loop

(Some figures may appear in colour only in the online journal)

1. Introduction

Many superconducting devices, such as SQUIDs, flux qubits, RSFQ circuits, etc, require biasing by magnetic flux for their optimal operation. Miniaturization of such superconducting circuits becomes difficult because ever higher magnetic fields need to be concentrated into smaller areas of superconducting loops. Furthermore, fluctuations of the bias fields can increase noise and disturb operation of the circuits. Integration of phase shifters can avoid the need for external current sources to generate high bias magnetic fields in nanoscale devices [1]. The role of a π-phase shifter can be played by a Josephson junction (JJ) with a ferromagnetic barrier (SFS-JJ) [2–5] or an island of a *d*-wave superconductor like the high-T_c superconductor $YBa_2Cu_3O_{7-x}$ (YBCO) that is contacted via a normal conducting gold layer along its [100] and [010] axes by an *s*-wave superconductor like the low-T_c superconductor

Nb (SNS *ds*-JJ) [6, 7]. As compared to SFS-JJs, *ds*-JJs are not magnetic and thus do not exhibit ferromagnetic hysteresis and Barkhausen noise.

An advantageous property for a phase shifter is a high critical current density J_c at 4.2 K, as that allows the flow of sufficiently strong spontaneously induced persistent currents in a superconducting loop that encloses such π-phase shifter (π-loop) to provide the condition $\beta_L = 2\pi I_c L/\Phi_0 >> 1$ also in the case of submicrometer wide *ds*-JJs. The reported maximal J_c of planar Nb–$Cu_{0.47}Ni_{0.53}$-Nb SFS-JJs in the π-state is about 1 kA cm^{-2} at 4.2 K [8] while J_c of ramp-type YBCO–Au–Nb (YBCO-Nb) *ds*-JJs made in the same deposition system and using similar parameters as the junctions reported below is about 5 kA cm^{-2} at 4.2 K [9]. The SFS JJs require a well-defined and relatively thick ferromagnetic layer and specific temperatures to change the sign of the order parameter. On the other hand, YBCO islands with *ds*-JJs operate as π-shifters in the entire temperature range below the superconducting transition temperature T_c and with Au-barrier thicknesses down to few nanometers.

Even higher values of J_c are expected for *ds*-JJs in which the Nb electrode would be replaced by a less oxidizing *s*-wave superconductor that has a larger superconducting energy gap. A prospective candidate for such an *s*-wave superconductor is a MoRe alloy that has a superconducting transition temperature T_c of up to 15 K [10] and at ordinary temperatures below 1000 °C it is much stronger corrosion and oxidation resistant than Nb and its alloys. The critical temperature of Mo_xRe_{1-x} films reaches the maximum value for the $Mo_{0.6}Re_{0.4}$ (MoRe) alloy [11].

In the present paper, we describe ramp-type YBCO–Au–MoRe (YBCO–MoRe) *ds*-JJs on graphoepitaxially buffered MgO substrates. This is the first time that the MoRe alloy is used as an *s*-wave superconductor in *ds*-JJs. For these *ds*-JJs, we investigated microstructural properties and measured *I(V)*-characteristics in different directions. The junctions were enclosed in π-loops of different shapes with different couplings to each other. Higher magnetic states of the π-loops beyond the $\pm 0.5\Phi_0$ ground states were induced by currents in integrated bias lines and stabilized at zero field.

2. Experimental details

Heterostructures of *ds*-JJs and π-loops were deposited on 10 mm × 10 mm × 1 mm MgO substrates by high-oxygen-pressure magnetron sputtering in pure (5 N) oxygen at pressure of 2 mbar and a substrate temperature 800 °C from stoichiometric polycrystalline targets of YBCO and $SrTiO_3$ (STO) [12, 13]. The surface of the substrates was cleaned by propanol and ion beam etching. A sufficiently long ion beam etching at an incident angle of 90° provides textured surfaces of the sample that facilitate graphoepitaxial growth of a double-layer buffer including about 2 nm of non-superconducting YBCO film and 10 nm of STO film [14, 15]. The base electrodes of the individual *ds*-JJs and all π-loops were made from 500 nm thick superconducting precipitate-free YBCO films covered by insulating 100 nm thick STO films.

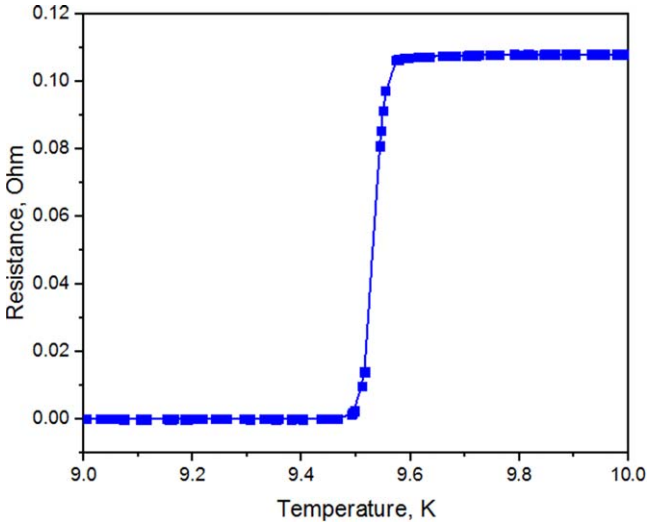

Figure 1. *R(T)*-dependence at the superconducting transition of a 200 nm thick MoRe film.

The layers of STO below and above the 500 nm thick superconducting YBCO layer are auxiliary insulating layers that do not transport the Josephson current.

The base electrode was patterned using a 2 μm thick reflowed mask of AZ TX1311 photoresist and Ar ion milling down to the MgO substrate at a 60° angle of incidence with the sample rotating around the axis normal to the surface of the substrate. The resulting edge of the base electrode has a slope angle of about 35° relative to the surface of the substrate. The rest of the photoresist was removed using acetone in ultrasonic bath and by an oxygen plasma. The surface of the edge was recovered by deposition of a 6 nm thick YBCO film [16]. Then a 3 nm or 6 nm thick gold barrier layer and a 200 nm thick MoRe top electrode were deposited *ex situ* at room temperature in an atmosphere of pure (5 N) Ar at pressure of 1 Pa using DC magnetron sputtering. Electrical contacts for application of bias currents and voltage measurements were made using pads that were sputtered through a metal mask along the edges of the substrate. The pads consist of a 20 nm thick Pt layer, which is covered with a 200 nm thick Ag film. Ag wires with a diameter of 100 μm were pressed onto the contact pads with indium pieces in order to establish a galvanic connection to the control electronics.

The superconducting transition temperature T_c of 200 nm thick MoRe films that are used for the top electrode and bias current lines was ≅9.5 K (see figure 1). This T_c is 1.4 K higher than T_c of the Nb films ≅8.1 K that were deposited at similar conditions and used in the *ds*-JJs with Nb top electrode in the previous study [9].

The top electrode together with the gold barrier layer were structured by Ar ion milling through a mask of AZ TX1311 or UV6-06 photoresist using a rotating substrate at a 10° angle of incidence to form the YBCO–MoRe *ds*-JJs. Individual 3 μm wide *ds*-JJs were prepared along the [100] (or [010]) and [110] axes of YBCO to investigate anisotropy of their critical current. We do not distinguish between the

[100] and [010] axes of YBCO because the YBCO films typically contains a twin structure with a period of approximately 30 nm [17]. The rest of the photoresist was removed by rinsing of the sample in acetone.

Microstructural properties of the junctions were investigated using a JEOL 7400 F scanning electron microscope (SEM) and a Philips CM-20 transmission electron microscope (TEM). Magnetic flux states of π-loops were observed using a low temperature scanning SQUID microscope (SSM) system [18, 19].

The two *ds*-JJs of each π-loop were oriented along the [100] or [010] crystallographic axes of YBCO. Different layouts of π-loops based on the novel *ds*-JJs were arranged in various mutual coupling configurations. Loops of current lines intended for manipulation of magnetic states of the π-loops were patterned in the MoRe layer in the vicinity of some π-loops. Contact pads for individual test-JJs and flux bias lines are arranged on the sides of the substrates and covered by a 10 nm thick Pt adhesion layer and 200 nm thick Ag films. Electrical contacts were made by Ag wires, pressed to the contacts pads by pieces of indium. The middle part of the samples was covered by a 2 μm thick mask of AZ 5214E photoresist to protect the π-loops from damage during measurements by SSM. The sensing area of the SQUIDs used in the SSM system is a pick-up loop of diameter 8 μm, separated from the SQUID washer by a relatively long shielded lead. The direct current (DC) SQUID in the SSM system is based on conventional Nb/AlOx/Nb trilayer junction technology. The magnetic field resolution of the SQUID at the pick-up loop area is approximately 40 pT/$\sqrt{\text{Hz}}$ and the flux noise typically $<2\,\mu\Phi_0/\sqrt{\text{Hz}}$ [18]. The SQUID was placed in the SSM measurement system below the sample on a flexible Kapton foil cantilever with patterned current leads at an angle of approximately 10° relative to the sample surface. In the measurement position the SQUID was mostly in a mechanical contact to the surface of the sample.

Current–voltage characteristics *I(V)* of individual *ds*-JJs were recorded using a home-made low-noise PC-controlled 4-terminal DC measurement system. Spontaneously induced magnetic fluxes of the π-loops were investigated using SSM with SQUID control electronics from the company STAR Cryoelectronics. The SSM runs on a LabVIEW script.

All measurements were performed at 4.2 K with the sample immersed in liquid helium. To reduce the background magnetic field to below 1 μT, the sample in the SSM system was magnetically shielded by a superconducting Nb cylinder and the helium cryostat was surrounded by a cylindrical μ-metal shield with a wrapped copper coil for compensation of vertical component of external magnetic field.

3. Results and discussion

SEM images of an individual *ds*-JJ and of two inductively coupled triangle π-loops with a flux bias line are shown in figures 2(a) and (b) respectively. The *ds*-JJs and the flux bias line are 3 μm wide. The use of pure Ar ion milling at the 10° angle of incidence lead to creation of 10 nm wide features (so-

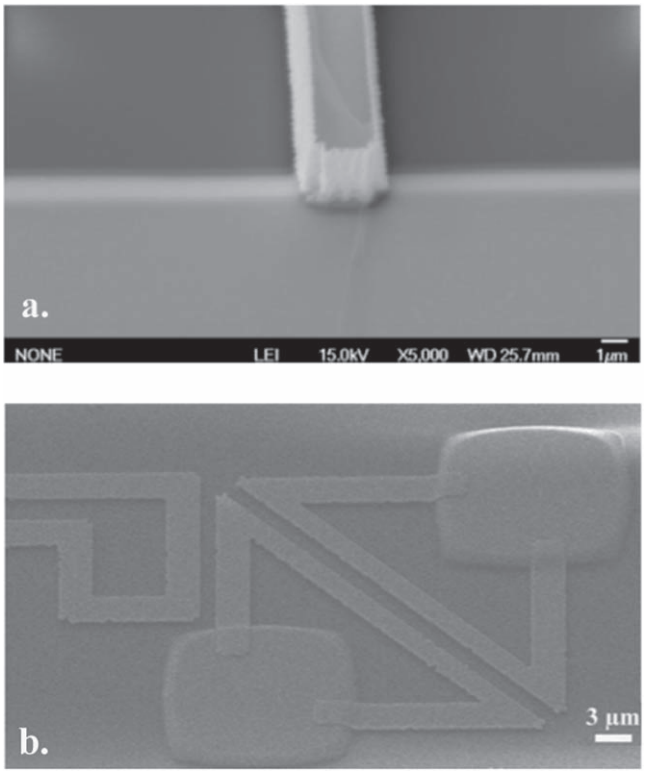

Figure 2. SEM images of (a) an individual YBCO–MoRe *ds*-JJ and (b) two inductively coupled triangle-shaped π-loops with 3 μm wide *ds*-JJs.

called 'fences' [20] or 'rabbit ears' [21]) at the edges of the top electrode. The height of the fences depends on the thickness of photoresist: for π-loops (figure 3(b)) mainly a much thinner UV6-06 photoresist was used to minimize variation of heights on the sample surface for more convenient SSM measurement. No fences on the edges of the bottom electrode were observed.

Cross-sectional SEM and TEM images of an individual YBCO–MoRe *ds*-JJ are shown in figures 3(a) and (b) respectively. Figure 3(b) shows the crystal structure of the boundary region between the superconducting YBCO layer and the top STO layer in the vicinity of the Au barrier and MoRe superconducting electrode. These images demonstrate the relative thicknesses of the involved films and epitaxial *c*-axis oriented growth of YBCO film up the barrier layer. Recrystallization of YBCO surface during deposition of the recovering YBCO film at 800 °C substrate temperature does not change the crystallographic orientation of the YBCO film including the crystallographic orientation of the recovering 6 nm thick YBCO film. In the TEM image presented in figure 3(b), the 3 nm thick gold barrier has a low contrast relative to the MoRe layer. No fences are visible in figure 3(a). The slope of the edge of the bottom electrode is about 35°.

The *I(V)*-characteristics of individual 3.3 μm wide YBCO–MoRe *ds*-JJs with a 3 nm thick Au barrier oriented along [100] or [010] crystallographic axes of YBCO are shown in figure 4(a). Figure 4(b) show *I(V)*-characteristic along the [110] axis of YBCO. The JJs that are oriented along

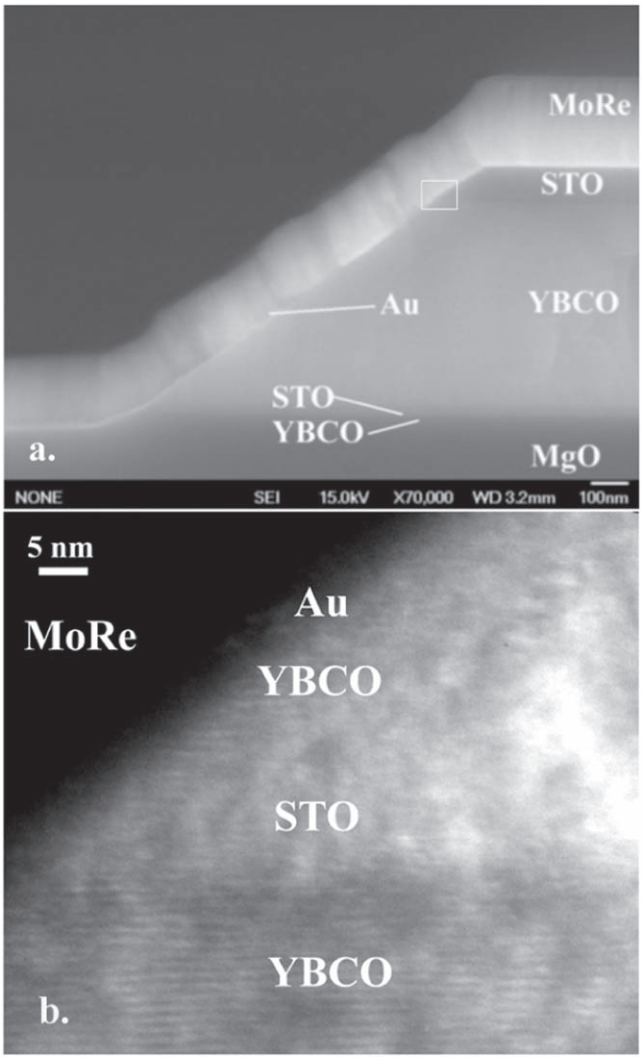

Figure 3. (a) SEM images of a cross-section of an individual YBCO–MoRe *ds*-JJ prepared on buffered MgO substrate and (b) a higher magnification TEM image of the selected in figure 3(a) area of the junction. In the TEM image the gold barrier layer has a low contrast relative to the top electrode MoRe layer.

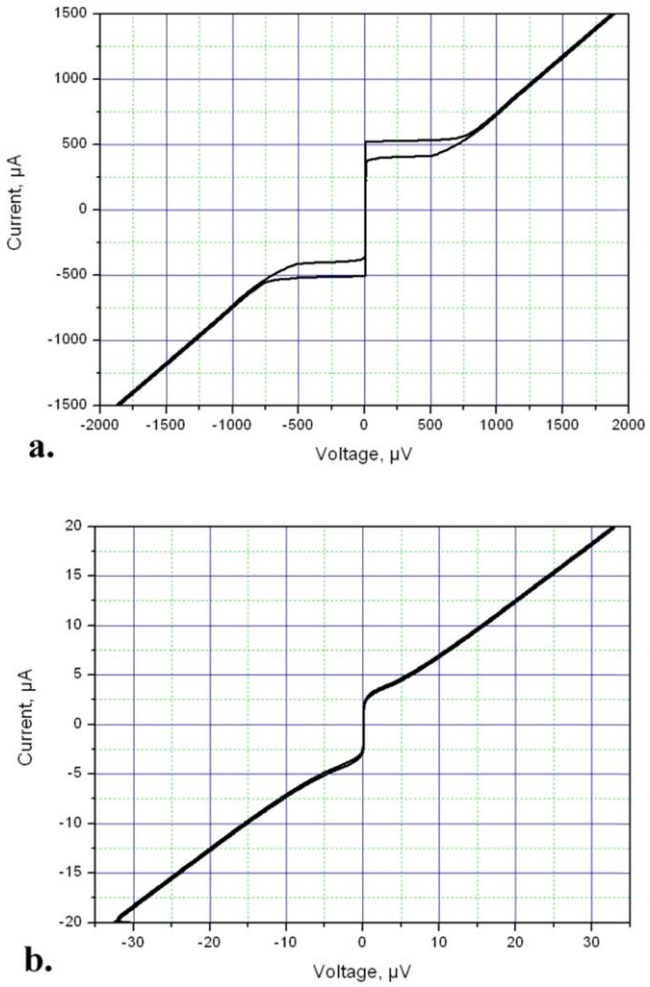

Figure 4. *I(V)*-characteristics of the individual 3.3 μm wide YBCO–MoRe *ds*-JJs with 3 nm thick Au barrier prepared (a) along the [100] or [010] crystallographic axes of YBCO and (b) along the [110] axis of YBCO. The characteristics were measured inside a μ-metal shield at 4.2 K.

the [100] or [010] axes of the YBCO film exhibit significant hysteresis with critical current $I_c \cong 500\ \mu$A and normal state resistance $R_n \cong 1.5$ Ohm. This critical current is a 200 times higher than the critical current of similar *ds*-JJs oriented along the [110] axis of the same YBCO film, which is consistent with the *d*-wave symmetry of the superconducting order parameter of YBCO. A critical current density $J_c = 20\ \text{kA cm}^{-2}$ at 4.2 K was achieved. Figure 4(a) shows *I(V)*-characteristic of the same junction that is shown in the SEM image in figure 2(a).

The high anisotropy of the *ds*-JJs is consistent with the *d*-wave symmetry of the order parameter in YBCO up to the interface with the barrier layer of the junctions. The YBCO films are not untwinned, which would require additional materials science tricks [22]. However, the superconducting order parameter does not change sign over twin-boundaries [6], which allows us to observe the effects of the *d*-wave symmetry of the order parameter in YBCO on a 10 μm scale, which is over 100 times larger than the width of twins in our YBCO films (see figure 5 in [17]). A value for the McCumber parameter $\beta_c \cong 2.6$ of the [100]-oriented *ds*-JJ was estimated from the amplitude of hysteresis of the *I(V)*-characteristics [23]. The corresponding capacitance C of the junctions is about 750 fF. For the π-loops we used JJs with 6 nm thickness of Au barrier and critical current $I_c = 165\ \mu$A at 4.2 K that have a better long-term stability of superconducting properties.

We have performed magnetometry measurements on a pair of triangular π-loops using the SSM (see figure 5). The central graph in figure 5 shows result of measurements in a fixed position over the middle of the π-loop during 50 sweeps of the current through the bias line between -15 mA and $+15$ mA. Switching of secondary π-loop 'II' of the pair due to magnetic field of the bias line is also detected by the SQUID and causes some small extra vertical bumps in the graph: one of them is indicated by red circle.

The top left insert in figure 5 shows the mask design of the related part of the sample with the location of the SQUID sensor (not to scale) indicated by a red point. The magnetic

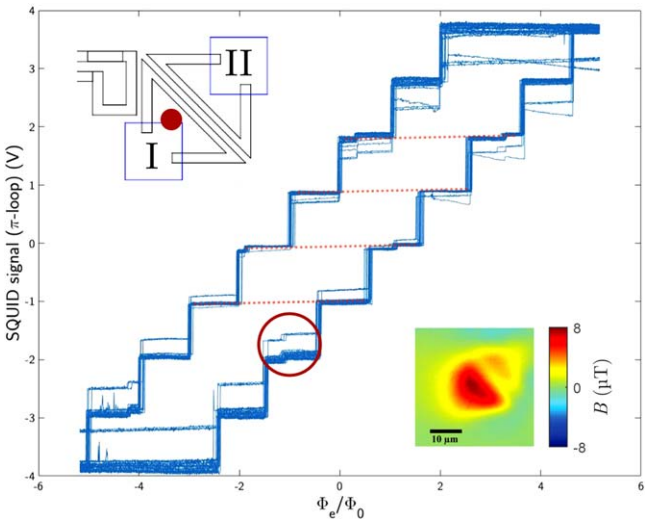

Figure 5. SQUID output voltage V, proportional to the magnetic field, measured by SSM in the middle of the loop as a function of applied current I through the bias current lines. The top left insert shows the mask design of the related part of the sample with the location of the SQUID sensor over the loop 'I' circled (not to scale). Bottom-right insert: 2D-distribution of the normal to the substrate surface B_z-component of the magnetic field measured by SSM over a pair of MoRe-based triangular π-loops, with the lower-left loop (I) in a higher flux state than the upper-right loop (II). The bias flux was subtracted from the SQUID signal.

fields originating directly from the bias line were subtracted from the output signal of the SSM. The current through the bias line was recalculated into the normalized magnetic flux that was generated by the bias line and penetrating the π-loop. The magnetic field of π-loop 'II' acts as an external field to the π-loop 'I'. This causes π-loop 'I' to switch at some point earlier/later and causes tiny horizontal shifts in the graph. The vertical bumps and horizontal shifts of the switching fields have some spreads due to residuals of electromagnetic noise from the environment and probabilistic nature of thermal activation over the barriers between the magnetic states of the π-loops. They are also not symmetric relative to the $\Phi_e = 0$ due to the residual background magnetic field.

The bottom-right insert in figure 5 shows a 2D-distribution of the B_z-component of the magnetic field over this pair of triangular π-loops. The lower-left π-loop generates a stronger magnetic field than the upper-right one. This indicates a higher magnetic field flux state of the lower-left π-loop compared to the flux state of the upper-right π-loop. By summing over both loops, we find a total flux of 2.5 Φ_0. Since both loops are in a positive state, theoretically, the possible combination should be that the lower-left loop is in the $+1.5\Phi_0$ and the upper-right in the $+0.5\Phi_0$ state, yielding a total flux of $2\Phi_0$. The discrepancy can be due to uncertainty in integration area because this scan was performed at the distance of approximately 5 μm from the substrate surface.

According to figure 5, the observed width of the hysteresis for the triangular π-loop $\Delta\Phi$ was about $2.8\Phi_0$. This value can be used for estimation of parameter β_L of this π-loop. The magnetic field generated by the applied current

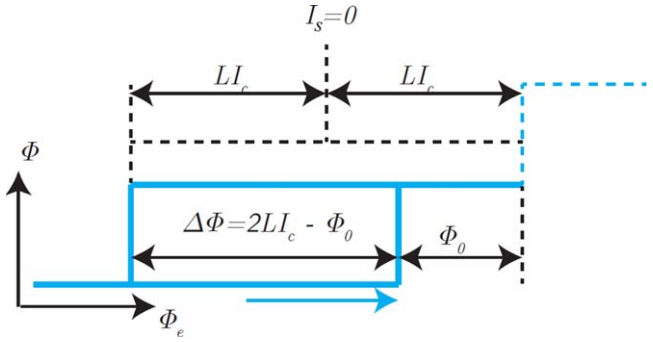

Figure 6. $\Phi(\Phi_e)$-diagram illustrating the relationship between the ΔH-hysteresis loop and the inductance of π-loop.

through the flux bias line forces the π-loop to switch to different magnetic state. The transition is happening when the induced superconducting current I_s in the loop is approaching critical current I_c of the *ds*-JJs. The maximal persistent current $I_s = I_c$ corresponds to a 'critical' magnetic flux $\Phi_c = I_cL$ that can be compensated ('screened') by the induced superconducting current I_s in the π-loop. The maximal range of the constant flux areas in π-loop is $2\Phi_c$.

Figure 6 shows a $\Phi(\Phi_e)$-diagram that illustrates the relation of the $\Delta\Phi$-hysteresis loop to the inductance of π-loop. The width of the hysteresis loop $\Delta\Phi$ is related to Φ_c by the expression: $\Delta\Phi = 2\Phi_c - \Phi_0$. In the case of monotonously increasing external flux Φ_e, the period of the step structure on the $\Phi(\Phi_e)$-dependence is Φ_0, corresponding to sequential penetration of single magnetic fluxes into the π-loop.

From the hysteresis loop the experimental value of the parameter $\beta_L = 2\pi\Phi_c/\Phi_0 = \pi(1 + \Delta\Phi/\Phi_0) \cong 12$. For a critical current $I_c = 165$ μA this corresponds to an inductance $L = \Phi_0/2\pi I_c \cong 24$ pH. The estimates that were made with the help of the software package 3D-MLSI [24] give inductance $L \cong 32$ pH for the triangle π-loop. The 25%-deviation of the calculated inductance from the measured one can be attributed to a spread of dimensions due to the limited spatial resolution of optical lithography of the π-loop and a simplified model that was taken for the calculation.

The condition for flux quantization in π-loop containing two junctions and the extra π-phase shift due to *d*-wave symmetry of the order parameter in YBCO results in the following phase-flux relation:

$$2\pi\Phi/\Phi_0 + \Delta\varphi_1 + \Delta\varphi_2 = \Delta\varphi_{\mathrm{YBCO}} + 2\pi n = (1 + 2n)\pi, \tag{1}$$

where $\Delta\varphi_1 = \Delta\varphi_2 = \Delta\varphi$ are the phase shifts on the JJs due to flow of the self-induced persistent superconducting current $I_s = I_c\sin(\Delta\varphi) = \Phi/L$ and $\Delta\varphi_{\mathrm{YBCO}} = \pi$ is the phase shift across YBCO between the [100]- and [010]-oriented *ds*-JJs. Using the relationships $\Phi = I_sL$ and $\Delta\varphi = \arcsin(I_s/I_c)$, we can rewrite the equation (1) as follows:

$$2\pi I_sL/\Phi_0 + 2\arcsin(I_s/I_c) = (1 + 2n)\pi. \tag{2}$$

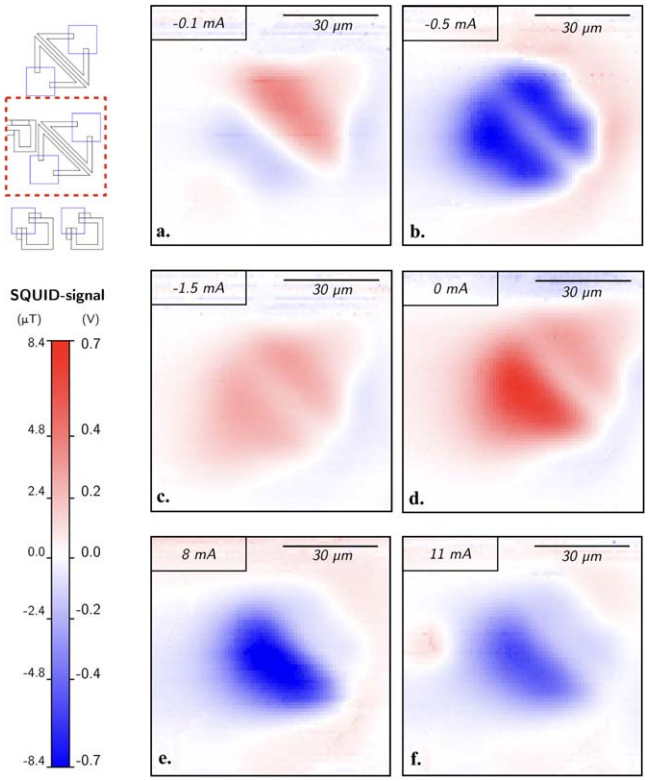

Figure 7. SSM-scans of a pair of triangular π-loops with 3 μm *ds*-JJs. Area: 75 μm $\times$ 75 μm, resolution: 75 px $\times$ 75 px, scanning speed: 50 μm s^{-1}, 3-point levelled. On the top left, the mask design of the scanning area is illustrated. The induction currents are indicated in the top left corners of the scans. The color scale at the bottom left represents the SQUID voltage and the corresponding local amplitude of the B_z component of the magnetic field.

For a sufficiently large screening parameter $\beta_L = 2\pi I_c L/\Phi_0 >> 1$, the second term on the left side of the equation (2) can be neglected resulting in values of $\Phi = I_s L = (n + 0.5)\Phi_0$. In the case of smaller I_c, still provided $\beta_L > 1$, the equation (2) was solved geometrically and resulted in values of Φ in the range $1 < |\Phi| < 1/2\Phi_0$. In the case when *ds*-JJs are used for optimal self-biasing of DC-SQUIDs, the flux bias $|\Phi| = 1/4\Phi_0$ is achieved at $2\arcsin(I_s/I_c) = \pi/2$ that would correspond to $I_s/I_c = \sin(\pi/4) \cong 1/\sqrt{2}$.

Figure 8 shows six SSM-scans of a pair of triangular π-loops with 3 μm wide *ds*-JJs. The scans are performed over a scan area of 75 μm $\times$ 75 μm with resolution of 75 pixels $\times$ 75 pixels using a scanning speed of 50 μm s^{-1}. The images were 3-point levelled using the 'Three Point Levelling' procedure within the data processing programme Gwyddion [25]. This procedure lets to mark three points in the image which all should be at the same level.

On the top left part of the figure 7 the mask design of the scanning area is illustrated. The bias current is zero during SSM measurement; the label in the top left corner of each scan indicates the maximum current of the sweep done right before the measurement. These images demonstrate switching of both π-loops in the pair at different values of bias flux.

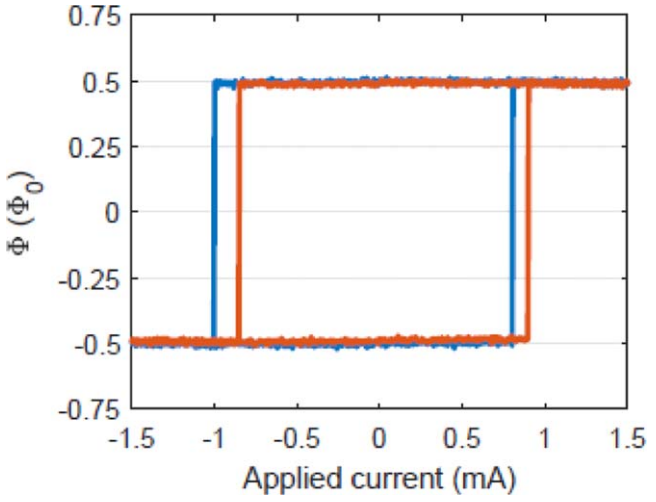

Figure 8. Comparison between two sweeps with the loop 'II' in different states.

Since the triangular loops came in a pair, we attempted to measure the coupling between these loops. By manipulating the loops using the bias line, we performed magnetometry measurements on one loop while having the second loop in either the $+0.5\Phi_0$ or the $-0.5\Phi_0$ state. We observed a clear shift along the horizontal axis, showing that the second loop does indeed influence the behavior of the first (see figure 8). We calculated the magnetic flux coupled from the second loop into the first to be $\sim 0.03\Phi_0$, while a simulation of the situation gave a value for magnetic flux of approximately $0.02\Phi_0$.

We also performed measurements on square π-loops with 6 μm wide *ds*-JJs. Thanks to the twice larger critical current of such junctions, we found that not only $\pm 0.5\Phi_0$ and $\pm 1.5\Phi_0$ states are stable in the absence of external flux Φ_e but also the states $\pm 2.5\Phi_0$ are stable, though the transition from them to $\pm 1.5\Phi_0$ lie very close to $\Phi_e = 0$. Transition between states is happening when the induced superconducting current in the π-loops reaches the critical current of at least one of the *ds*-JJs. Accordingly, the number of stable states at $\Phi_e = 0$ is $2\text{round}(I_c L/\Phi_0)$.

Figure 9 shows a hysteresis loop of a square π-loop with 6 μm *ds*-JJs measured by the SSM as a function of applied magnetic flux. The bias flux was subtracted from the SQUID signal. The insert shows the mask design of the related part of the sample with the location of the SQUID sensor (not to scale) circled. Since the free energy U is symmetric around $\Phi_e = 0$, an even number of stable states is expected. This means that there is a non-zero external magnetic flux Φ_e that changes the energy landscape and causes a shift of the magnetometry measurement along the horizontal axis. A residual background field up to $\sim 1\,\mu$T would produce magnetic flux up to only 5 mΦ_0 through the π-loop of 10 μm^2 area.

The free energy U of a π-loop with two *ds*-JJs has the following dependence on magnetic flux Φ in the presence of

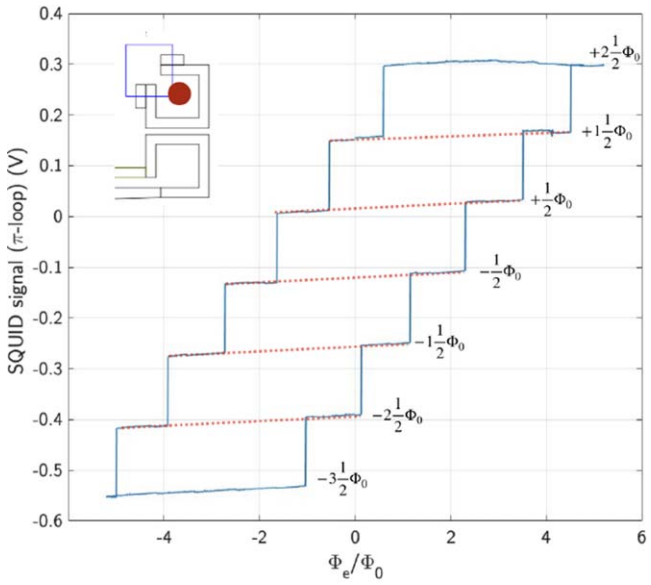

Figure 9. Hysteresis loop of a square π-loop with 6 μm *ds*-JJs measured by the SSM as a function of applied magnetic flux. The bias flux was subtracted from the SQUID signal. Insert shows the mask design of the related part of the sample with the location of the SQUID sensor (not to scale) circled.

the external flux Φ_e through the π-loop:

$$U(\Phi, \Phi_e) = \frac{(\Phi - \Phi_e)^2}{2L} - E_{J1}\sqrt{1 + \gamma^2 - 2\gamma\cos\left(\frac{2\pi\Phi}{\Phi_0}\right)}, \tag{3}$$

where $\gamma = I_{c1}/I_{c2}$, I_{c1} and I_{c2} are critical currents of the *ds*-JJs and $E_{J1} = \Phi_0 I_{c1}/2\pi$ is the Josephson energy.

At $\Phi_e = 0$ the free energy has two total minima at $\Phi = \pm 0.5\Phi_0$ that leads to the spontaneous appearence of the magnetic flux and persistent current of two possible directions that correspond to the two energetically equivalent states. Figure 10 shows theoretical dependence of free energy $U(\Phi)$ for π-loop with equal critical currents $I_{c1} = I_{c2}$ of the *ds*-JJs and the external flux $\Phi_e = 0$:

$$U(\Phi, \Phi_e) = \frac{\Phi^2}{2L} - \frac{\Phi_0 I_c}{2\pi}\sqrt{2 - 2\cos\left(\frac{2\pi\Phi}{\Phi_0}\right)}. \tag{4}$$

The free energy of π-loops with different *ds*-JJs was estimated according to the equation (2) and the results are presented in figure 11. Curve 1 represents the calculated free energy of π-loops with 3 μm wide YBCO-Nb *ds*-JJs using their I_c and L values from [9]. Curve 2 and 3 represent calculated free energies of π-loops with 3 μm wide YBCO–MoRe *ds*-JJs (curve 2) and 6 μm wide YBCO–MoRe *ds*-JJs (curve 3), respectively. The energy barrier between $1.5\Phi_0$ and $2.5\Phi_0$ states E_{b3} for π-loops with 6 μm wide YBCO–MoRe *ds*-JJs is strong enough to stabilize $2.5\Phi_0$ states against thermal fluctuations: $E_{b3} \cong 1800\ k_BT$ at 4.2 K. For π-loops with 3 μm wide YBCO-Nb *ds*-JJs $E_{b2} \cong 14\ k_BT$ at 4.2 K while E_{b1} for π-loops with 3 μm wide YBCO-Nb *ds*-JJs and E_{b2} for π-loops with 3 μm wide YBCO–MoRe *ds*-JJs are both approximately $800k_BT$ at 4.2 K.

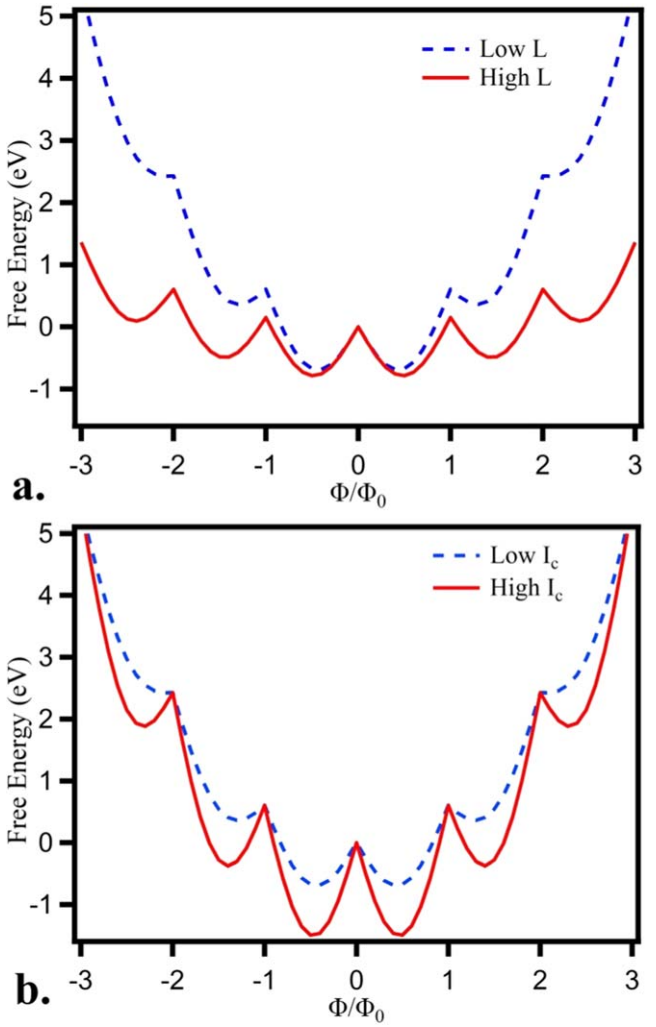

Figure 10. Theoretical dependences of free energy U of π-loops that have equal critical currents $I_{c1} = I_{c2}$ of the *ds*-JJs in the case of $\Phi_e = 0$ with variations in the (a) inductance and (b) critical current. The magnetic flux in the π-loops Φ is normalized in units of Φ_0.

Application of bias flux $\Phi_e \neq 0$ makes other states energetically more favourable and changes the height of the energy barrier between states. At 4.2 K, transitions to other states are happening when the barrier is at least smaller than the thermal energy k_BT. Reduction of temperature can lead to the situation that quantum tunneling through the energy barrier becomes more probable compared to the thermal activation over the energy barrier (see figure 12). Such quantum dynamics of the π-loops with the *ds*-JJs considered here would be a new realization of a macroscopic quantum tunneling (MQT) effect that could be potentially useful for implementation in prospective 'quiet' qubits [26].

In the following we discuss conditions for realization of MQT in *ds*-JJs. The crossover temperature T^*, at which quantum tunneling starts to dominate the transition from non-voltage to voltage state, was calculated based on the theoretical work of Kawabata *et al* [27]. In experiment, the crossover temperature T^*, at which the transition occurs from the classical thermal activation (TA) to the quantum tunneling (QT) regime, can be determined by doing switching current

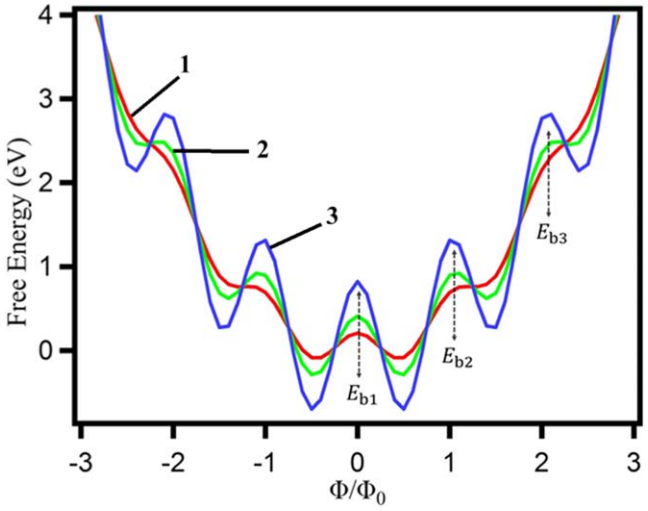

Figure 11. Free energy calculated for π-loops with 3 μm wide YBCO-Nb *ds*-JJs (curve 1) using their I_c and L values from [9], 3 μm wide YBCO–MoRe *ds*-JJs (curve 2) and 6 μm wide YBCO–MoRe *ds*-JJs (curve 3). E_{b1}—energy barrier between $-0.5\Phi_0$ and $0.5\Phi_0$ states, E_{b2}—energy barrier between $0.5\Phi_0$ and $1.5\Phi_0$ states, and E_{b3}—energy barrier between $1.5\Phi_0$ and $2.5\Phi_0$ states.

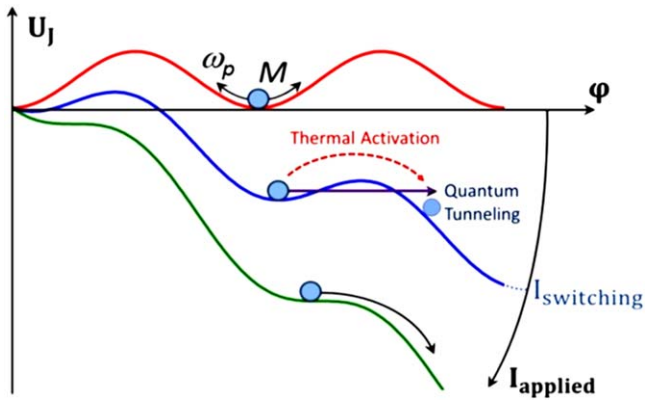

Figure 12. Transitions between states in a Josephson junction due to classical thermal activation and quantum tunneling at a threshold value $I_{switching}$ of the induced persistent current in the π-loop.

distribution experiments as a function of temperature (see, for example, [28]). Below is the equation for distribution of switching current $P_{switching}$ with the function of applied bias current $I_{applied}$ when the transition from the non-voltage to the voltage state happens:

$$P_{switching}(\eta) = \frac{1}{v}\Gamma(\eta)\exp\left[-\frac{1}{v}\int_0^{\eta}\Gamma(\eta')d\eta'\right], \quad (5)$$

where η is the normalized applied current $I_{applied}/I_c$ and $v = |d\eta/dt|$ is the sweep rate of the applied current. At high temperatures, the thermally activated (TA) decay dominates the escape process. Then, the escape rate is given by the Kramers formula:

$$\Gamma_T(\eta) = \frac{\omega_p}{2\pi}\exp\left[-\frac{U_0}{k_B T}\right], \quad (6)$$

where ω_p—plasma frequency, $E_J = \Phi_0 I_c/2\pi$ and U_0—the barrier height of the washboard potential energy:

$$U_0 = 2E_J\{\sqrt{1-\eta^2} - \eta[\arccos(\eta)]\}. \quad (7)$$

For the quantum tunneling regime, especially in the case of Josephson junctions based on *s*-wave/*d*-wave superconductors, the estimation for the escape rate is complicated by the effect of low-energy quasiparticles, such as the nodal quasiparticles and the zero energy bound states. Kawabata *et al* [27] derived that in realistic hybrid *ds*-JJs the quantum tunneling rate will be:

$$\Gamma_Q(\eta) = \frac{\omega_p(\eta)}{2\pi}\sqrt{120\pi B(\eta)}\exp\left[-B(\eta) - \frac{54\xi(3)R_Q}{\pi^4 R_s}(1-\eta^2)\right],$$

where:

$$\omega_p(\eta) = \sqrt{\frac{\hbar I_c}{2eM}}(1-\eta^2)^{1/4}$$

and

$$B(\eta) = \frac{12}{5e}\sqrt{\frac{2e}{\hbar}I_c M(1-\eta^2)^{5/4}},$$

with M—the mass $C(\hbar/2e)^2$, R_n—the normal state resistance of the junction, C—capacitance of the junction, and $R_Q = h/4e^2 = 6.45$ kOhm is the resistance quantum. For *ds*-JJs oriented along one of the lobes directions [100] or [010], $\Gamma_Q(\eta)$ has finite values. In the case of the orientation of the junction along a nodal direction [110] critical current I_c of the junction nearly zero and hence the $\Gamma_Q(\eta)$ is also nearly zero.

By equating numerically the standard deviation of switching distribution $P^{TA}_{switching}(\eta)$ and $P^{QT}_{switching}(\eta)$, $\sigma_T \approx \sigma_Q$, the crossover temperature T^*—the temperature threshold at which the quantum regime starts to take over, can be calculated [27]. Junction parameters and numerical calculation parameter used for calculation of $P_{switching}(\eta)$ for the fabricated *ds*-JJ (width $w = 3.3$ μm, thickness $d_{YBCO} = 0.5$ μm): $I_c = 500$ μA, $R_n = 1.33$ Ohm, $C = 750$ fF, and sweep rate $I_c\frac{d\eta}{dt} = 0.0424$. The results of the simulations are shown in figure 13 A crossover temperature $T^* \cong 0.138$ K was obtained.

The crossover temperature $T^* \cong \omega_0/k_B T \propto \sqrt{(I_c/C)}$, where ω_0 is the oscillation frequency of the particle at the bottom of the well [27, 29]. The critical current slightly increases with reduction of temperature below 4.2 K: $I_c(<2\text{ K}) \cong 1.2 \times I_c(4.2\text{ K})$ [9] according to the dirty weak link behavior of *ds*-JJs described by the Kulik–Omelyanchuk theory (see, for example, a review [30] and references therein). Accordingly, the real TA-QT crossover temperatures can be approximately 10% higher than the performed numerical estimates that were calculated using a fixed value of critical current I_c.

A significant miniaturization of *ds*-JJs at least down to about area $A = 200\text{ nm} \times 200\text{ nm}$ seems to be possible: figure 14 shows an SEM image of a π-loop with $200\text{ nm} \times 700\text{ nm}$ Nb *ds*-JJs.

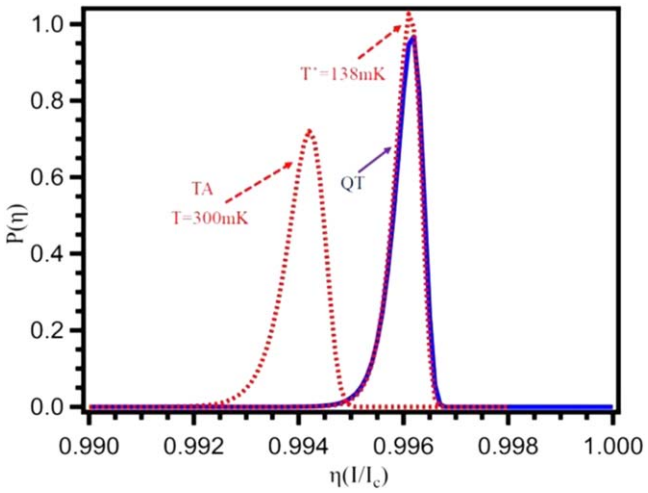

Figure 13. Theoretical estimations of the transition temperature from classical thermal activation (TA) to quantum tunneling (QT) modes performed for the 3.3 μm wide YBCO–MoRe *ds*-JJs.

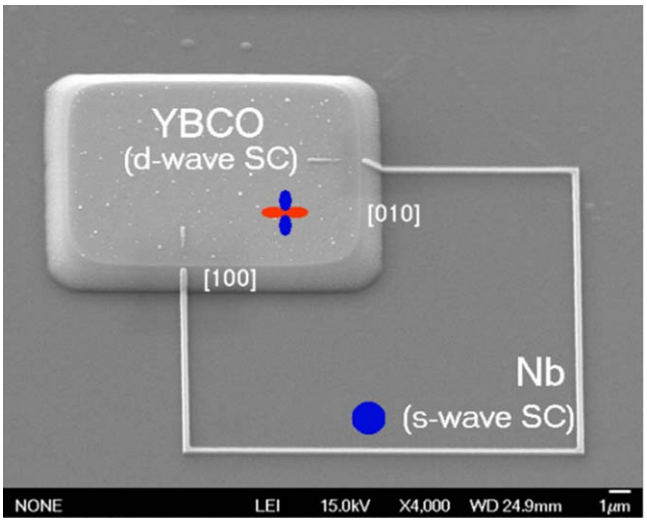

Figure 14. SEM image of a π-loop with 200 nm $\times$ 700 nm YBCO-Nb *ds*-JJs produced with the help of an e-beam lithography.

The results of the numerical estimations for the *ds*-JJs of the area 0.04 μm^2 are shown in figure 15. Junction parameters and numerical calculation parameter used for calculation of $P_{switching}(\eta)$ for hypothetical YBCO–MoRe JJ ($w = 0.2$ μm, $d_{YBCO} = 0.2$ μm): $I_c = 12$ μA, $R_n = 55$ Ohm, $C = 18.4$ fF, and sweep rate $I_c\frac{d\eta}{dt} = 0.0424$. The obtained crossover temperature $T^* \cong 0.6$ K would allow to use for observation of MQT a much simpler refrigerator technique based on evaporation of He^3 with a much higher cooling power at 500 mK compared to He^3/He^4-dilution refrigeration that is currently used for cooling of superconducting qubits. But in the case of application of the *ds*-JJs in qubits, it will be necessary to operate qubits at few tens of millikelvin temperatures: see the related numerical estimates below.

There are several potential possibilities to use π-loops for quantum sensing and information technology. They will help to avoid the need for external current sources to generate magnetic flux bias in nanoscale superconducting devices that

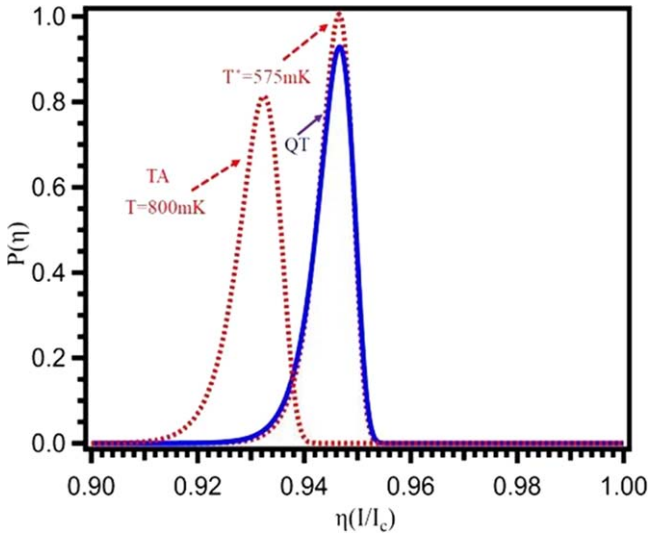

Figure 15. Theoretical estimations of transition temperature from thermal activation (TA) to quantum tunneling (QT) modes for hypothetical YBCO–MoRe *ds*-JJs that have junction area 200 nm $\times$ 200 nm.

requires local generation of relatively high magnetic fields: nanoSQUIDs of areas of the SQUID loop $A < 1$ μm^2 need to be biased by local magnetic field $B > 0.25\Phi_0/A \cong 0.5$ mT.

DC π-SQUIDs based on two *ds*-JJs were realized (see, for example, [31]). For magnetic field measurement the optimal flux bias of DC SQUID is $0.25\Phi_0$ where the derivative $\partial V/\partial F$ reaches its maximal value. DC SQUIDs with built-in switchable $\pi/2$-phase shift were made in a construction that includes ten *ds*-JJs [32]. For the sake of miniaturization of self-biased nanoscale DC SQUID magnetometers number of junctions should be reduced to two *ds*-JJs. In this case, the flux bias $|\Phi| = 0.25\Phi_0$ can be achieved by using a phase drop on each *ds*-JJ $\arcsin(I_s/I_c)$: according to the phase-flux relation (1) total phase drop on the two *ds*-JJs $2\arcsin(I_s/I_c) = \pi/2$ would correspond to the spontaneously induced normalized persistent current I_s through each *ds*-JJ in the π-loop of the SQUID $I_s/I_c = \sin(\pi/4) \cong 1/\sqrt{2}$. The required critical current I_c of the *ds*-JJs can be adjusted by area of the junctions and thickness of the barrier layer.

Currently, it is still necessary to realize such $\pi/2$-SQUIDs based on just two *ds*-JJs and measure their noise properties. Preferred orientation of the spontaneously induced flux would depend on the orientation of tiny background magnetic fields during cooling of the SQUID that are inherent for the typical measurement conditions. Alternatively, this preferred orientation can be established in a controlled manner by using injection of current for a tiny flux bias $\Delta\Phi << \Phi_0/4$ directly into the loop of the $\pi/2$-SQUID.

The residual background magnetic fields that determine orientation of spontaneously induced fractional magnetic flux quantum states $\pm 0.5\Phi_0$ in the π-loops is extremely low and comparable with the level of fluctuations of magnetic fields due to electromagnetic interference, thermal effects or quantum fluctuations that are always present in measurement system inspite of using of any sofisticated magnetic shielding.

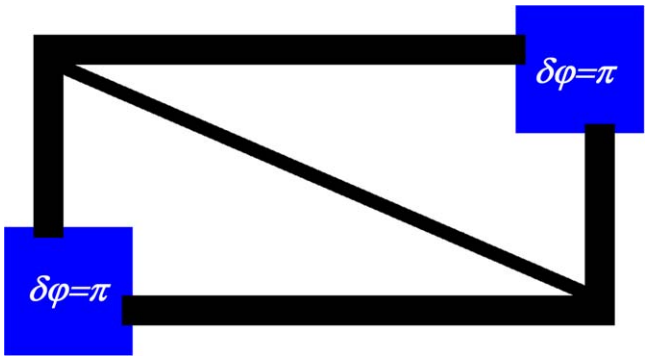

Figure 16. Schematics of two gradiometrically coupled π-loops with the *ds*-JJs. Such configuration should be less sensitive to fluctuations of background magnetic fields.

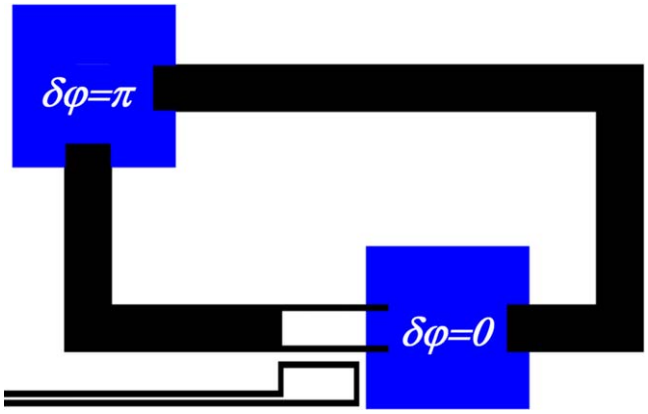

Figure 17. Schematics of an example of a quiet qubit based on a π-shifter with high-I_c *ds*-JJs and an effective controllable low-I_c *ds*-JJ in the form of a DC SQUID. YBCO electrodes are shown in blue color while *s*-wave superconductor (e.g. Nb or MoRe) electrodes are shown in black color.

Partially, the influence of the residual magnetic fields can be reduced by strong gradiometric coupling of a pair of π-loops as it is shown in figure 16.

The sensitivity of magnetic states of π-loops to tiny fields during thermal or quantum cooling and their self-biasing to optimal value of magnetic flux lead to a possibility to apply π-loops for computational purposes. Self-biased flux qubits ('quiet qubit') using π-loop with *ds*-JJs have potentially the longest coherence time because they are naturally decoupled from perturbations produced by the environment: their double-well potential with two degenerate states is symmetrized by the spontaneously self-induced persistent current instead of using an external current source. We have not estimated the coherence time in the suggested designs of the 'quiet' qubits: the resulting coherence time depends on other sources of decoherence that are present in the qubits and their environment and should be measured in the future experiments.

The demonstrated ability to stabilise and manipulate states of π-loops paves the way towards new computing concepts such as quantum annealing computing. Switching between the energetically equal states $\pm 0.5\Phi_0$ of the π-loops can be performed by application of a tiny bias of external magnetic flux accompanied with temporary decrease of potential barrier ('annealing') between the states down to a value at which thermal activation or quantum tunneling processes could take place. Critical current in the π-loop can be limited by a 'compound Josephson junction' made in the form of a DC SQUIDs [33] that has a critical current controllable by magnetic flux. The potential barrier between states is proportional to the Josephson energy or to the critical current of the Josephson junctions in the π-loop so that the tuning of the barrier height during the annealing process can be performed by heating of the sample or a controlled decrease of critical current of the compound Josephson junction that is controlled by local magnetic field of an integrated coil [33].

The compound Josephson junction for tuning of the barrier hight in the π-loop can be made in the same technological process (see figure 17). Critical currents of *ds*-JJs in the compound Josephson junction of the qubit should be much smaller than critical currents of the other *ds*-JJs in this circuit to reduce phase drop in that *ds*-JJs. In this case the screening parameter β_L of the qubit is determined by the inductance of the loop and the controllable critical current of the compound Josephson junction. At sufficiently low temperature and small tunnel barrier between states, the system can tunnel between states and reside in superposition of both states. Such qubits are expected to have a longer decoherence time because application of external magnetic flux bias would not be necessary. A numerical estimate according to the equation (17) in [29] for the *ds*-JJs, which would have an atteinable area 0.005 μm^2, gives a reasonable value for the energy gap of the tunnel splitting $\Delta_t \cong 39\,\mathrm{mK}\cdot k_B \cong h \times 0.8\,\mathrm{GHz}$, where $h \cong 6.6 \times 10^{-34}$ $J{\cdot}s$ is the Planck's constant.

A computation process in the case of quantum annealing at sufficiently low temperatures would involve reduction of tunnel barriers of the qubits that would enable their quantum entanglement and fast quantum computing resulting in final states that will be protected by high tunnel barriers between states after increase of critical currents. After that, the magnetic states of the π-loops can be read by SSM non-destructively and with sufficient resolution. Efficiency of the quantum computing based on the quantum annealing process can be potentially improved by implementation of self-biased flux qubits that have potentially longer coherence time because they are naturally decoupled from perturbations produced by the environment: their double-well energy potential is symmetrized by integration of a π-phase shifter in the loop of the flux qubit instead of using a conventional inductance with an external current source.

The first qubit based on *s*-wave/*d*-wave architectures with a π-phase-shift was theoretically proposed already 20 years ago [26] but it still faces a challenge to be proven whether the use of *d*-wave superconductors, with its nodal quasiparticles, always gives rise to excessive decoherence and would be detrimental for the qubit operation. It was shown theoretically [34] that the decoherence time of the *d*-wave/*d*-wave superconductor qubit is reduced due to the nodal quasiparticles. The *d*-wave/*d*-wave Josephson junctions, which were considered in [34], were with in-plane symmetric misorientation angles $\pm\alpha$ that are not too close to 0^o. Contribution of the nodal

quasiparticles to electron transport properties of the junctions would be significantly suppressed in the case of $\alpha = 0^{o}$: in the present study we use for π-loops the *ds*-JJs that are directed strictly along [100] or [010] crystallographic axes of the YBCO film and observed that critical current of such Josephson junctions is very different compared to the junctions in the direction of the [110] axis of the same YBCO film. In addition to that, it was also theoretically shown that on account of the quasiparticle-tunneling blockade effect in the *s*-wave/*d*-wave Josephson junctions, the decoherence time of the *s*-wave/*d*-wave qubit is expected to be much longer than that of the *d*-wave/*d*-wave qubits [27]. But this proposition still needs to be experimentally verified.

Scalability of the devices based on YBCO–MoRe *ds*-JJs is sufficiently good for preparation of large arrays of π-loops for production of quantum processors [33] or metamaterials [35, 36]. The ramp type YBCO–MoRe *ds*-JJs can be laid out in any place on a substrate and fabricated with small spread of parameters. Rectangular arrays of up to 40 000 π-loops based on YBCO-Nb *ds*-JJs were produced within an area 2 mm × 2 mm and reported in the [9]. Similar arrays can be produced with YBCO–MoRe *ds*-JJs. MgO wafers of over 10 cm × 10 cm are commercially available. This makes potentially possible to produce planar arrays of over 10^8 π-loops on a single chip.

4. Summary

Novel Josephson junctions between the *d*-wave superconductor YBCO and the *s*-wave MoRe-alloy superconductor (*ds*-JJs) on graphoepitaxially buffered MgO substrates were developed. MoRe alloy that has a superconducting transition temperature T_c of up to 15K [10] and at ordinary temperatures below 1000 °C it is much stronger corrosion and oxidation resistant than Nb and its alloys [37]. The characteristic voltage I_cR_n of the YBCO–MoRe *ds*-JJs with 3 nm Au barrier is approximately 750 μV at 4.2 K. The junctions oriented along the [100] or [010] crystallographic axes of the YBCO film exhibit a 200 times higher critical current than similar ds-JJs oriented along the [110] axis of the same YBCO film. A critical current density $J_c = 20\,\mathrm{kA\,cm^{-2}}$ at 4.2 K was achieved. Different layouts of π-loops based on the novel *ds*-JJs were arranged in various mutual coupling configurations. Spontaneously induced magnetic fluxes of the π-loops were investigated using scanning SQUID microscopy. Magnetic states of the π-loops were manipulated by currents in integrated bias lines. Higher magnetic field flux states up to $\pm 2.5\Phi_0$ were induced and stabilized in the π-loops. The demonstrated ability to stabilise and manipulate different fractional magnetic field flux quanta states of the π-loops paves the way towards their use for information technology, for example, for quantum annealing computing. The crossover temperature T^* between thermally activated and quantum tunneling switching processes as well as the energy gap of the tunnel splitting in the proposed 'quiet' qubits were estimated. The resulting coherence time in the suggested designs of the 'quiet' qubits will depend on other sources of decoherence that are present in the qubits and their environment and should be measured in the future experiments.

Acknowledgments

This work was supported in part by the PGI-5 FZJ CEI E-Project (E.23102.76). V S S and A A G are acknowledging support by the RFBR (project No. 19-52-50026).

ORCID iDs

M I Faley https://orcid.org/0000-0003-2768-2796
V S Stolyarov https://orcid.org/0000-0002-5317-0818
A A Golubov https://orcid.org/0000-0001-5085-5195
H Hilgenkamp https://orcid.org/0000-0001-6109-8804
R E Dunin-Borkowski https://orcid.org/0000-0001-8082-0647

References

[1] Hilgenkamp H 2008 *Supercond. Sci. Technol.* **21** 034001
[2] Ryazanov V V, Oboznov V A, Rusanov A Y, Veretennikov A V, Golubov A A and Aarts J 2001 *Phys. Rev. Lett.* **86** 2427
[3] Bannykh A A, Pfeiffer J, Stolyarov V S, Batov I E, Ryazanov V V and Weides M 2009 *Phys. Rev.* B **79** 054501
[4] Feofanov A K *et al* 2010 *Nat. Phys.* **6** 593
[5] Shcherbakova A V *et al* 2015 *Supercond. Sci. Technol.* **28** 025009
[6] Van Harlingen D J 1995 *Rev. Mod. Phys.* **67** 515–35
[7] Hilgenkamp H, Ariando, Smilde H-J H, Blank D H A, Rijnders G, Rogalla H, Kirtley J R and Tsuei C C 2003 *Nature* **422** 50
[8] Oboznov V A, Bol'ginov V V, Feofanov A K, Ryazanov V V and Buzdin A I 2006 *Phys. Rev. Lett.* **96** 197003
[9] Faley M I, Reith P, Stolyarov V S, Golovchanskiy I A, Golubov A A, Hilgenkamp H and Dunin-Borkowski R E 2019 *IEEE Trans. Appl. Supercond.* **29** 1100405
[10] Gavaler J R, Janocko M A and Jones C K 1972 *Appl. Phys. Lett.* **21** 179
[11] Deambrosis S M, Keppel G, Ramazzo V, Roncolato C, Sharma R G and Palmieri V 2006 *Physica* C **441** 108
[12] Poppe U *et al* 1992 *J. Appl. Phys.* **71** 5572
[13] Faley M I and Poppe U 2016 *Patent* US 9.481,928 B2
[14] Faley M I 2017 *Patent* US 9,666,783 B2
[15] Faley M I, Dammers J, Maslennikov Y V, Schneiderman J F, Winkler D, Koshelets V P, Shah N J and Dunin-Borkowski R E 2017 *Supercond. Sci. Technol.* **30** 083001
[16] Smilde H J H, Hilgenkamp H, Rijnders G, Rogalla H and Blank D H A 2002 *Appl. Phys. Lett.* **80** 4579–81
[17] Faley M I, Jia C L, Poppe U, Houben L and Urban K 2006 *Supercond. Sci. Technol.* **19** S195
[18] Kirtley J R, Ketchen M B, Stawiasz K G, Sun J Z, Gallagher W J, Blanton H and Wind S J 1995 *Appl. Phys. Lett.* **66** 1138
[19] Kirtley J R and Wikswo P 1999 *Annu. Rev. Mater. Sci.* **29** 117
[20] Philipsen V *et al* 2017 *J. Micro/Nanolith. MEMS MOEMS* **16** 041002

[21] Sung S, Kim C-H, Lee J, Jung J-Y, Jeong J-H, Choi J-H and Lee E-S 2014 *Int. J. Precis. Eng. Manuf.-Green Technol.* **1** 25–30
[22] Smilde H J H, Golubov A A, Ariando, Rijnders G, Dekkers J M, Harkema S, Blank D H A, Rogalla H and Hilgenkamp H 2005 *Phys. Rev. Lett.* **95** 257001
[23] Chen Y C, Fisher M P A and Leggett A J 1988 *J. Appl. Phys.* **64** 3119
[24] Khapaev M M, Kupriyanov M Y, Goldobin E and Siegel M 2003 *Supercond. Sci. Technol.* **16** 24
[25] Nečas D and Klapetek P 2012 Gwyddion: an open-source software for SPM data analysis *Central Eur. J. Phys.* **10** 181–8
[26] Ioffe L B, Geshkenbein V B, Feigel'man M V, Fauchere A L and Blatter G 1999 *Nature* **398** 679
[27] Kawabata S, Golubov A A, Ariando, Verwijs C J M, Hilgenkamp H and Kirtley J R 2007 *Phys. Rev.* B **76** 064505
[28] Bauch T, Lombardi F, Tafuri F, Barone A, Rotoli G, Delsing P and Claeson T 2005 *Phys. Rev. Lett.* **94** 087003
[29] Wallraff A, Lukashenko A, Coqui C, Kemp A, Duty T and Ustinov A V 2003 *Rev. Sci. Instrum.* **74** 3740
[30] Golubov A A, Kupriyanov M Y and Il'ichev E 2004 *Rev. Mod. Phys.* **76** 411
[31] Smilde H-J H, Ariando, Blank D H A, Hilgenkamp H and Rogalla H 2004 *Phys. Rev.* B **70** 024519
[32] Smilde H-J H, Ariando, Rogalla H and Hilgenkamp H 2004 *Appl. Phys. Lett.* **85** 4091
[33] Lanting T *et al* 2014 *Phys. Rev.* X **4** 021041
[34] Fominov Y V, Golubov A A and Kupriyanov M Y 2003 *Pis'ma v ZhETF* **77** 691
[35] Jung P *et al* 2014 *Nat. Commun.* **5** 3730
[36] Kalhor *et al* 2017 *IEEE Photonics J.* **9** 1400308
[37] El-Genk M S and Tournier J-M 2005 *Journal of Nuclear Materials* **340** 93–112